NC-AFM contrast formation on the calcite ($10\bar{1}4$) surface

2012 J. Phys.: Condens. Matter 24 084006

(http://iopscience.iop.org/0953-8984/24/8/084006)

J. Phys.: Condens. Matter **24** (2012) 084006 (14pp) doi:10.1088/0953-8984/24/8/084006

NC-AFM contrast formation on the calcite ($10\bar{1}4$) surface

Philipp Rahe, Jens Schütte[1] and Angelika Kühnle

Johannes Gutenberg-Universität Mainz, Institut für Physikalische Chemie, Jakob-Welder-Weg 11, D-55099 Mainz, Germany

E-mail: rahe@uni-mainz.de

Received 18 September 2011, in final form 4 November 2011
Published 7 February 2012
Online at stacks.iop.org/JPhysCM/24/084006

Abstract

Calcite, the most stable polymorph of calcium carbonate, is one of the most abundant simple salts in the geological environment. Consequently, its natural ($10\bar{1}4$) cleavage plane has been studied extensively by a wide range of surface-sensitive techniques, giving indications for two reconstructions, namely a (2×1) and a so-called 'row-pairing' reconstruction. The existence of the (2×1) reconstruction has been discussed controversially in the literature, but is now confirmed as a true surface property. In contrast, a comprehensive discussion on the existence of the row-pairing reconstruction is lacking so far.

Here, we present a non-contact atomic force microscopy (NC-AFM) study of the ($10\bar{1}4$) calcite surface performed in an ultra-high vacuum. We discuss a broad variety of different NC-AFM contrasts and present a comprehensive classification scheme. This scheme encompasses a total of 12 different contrast modes. Atomically resolved NC-AFM images are shown, giving experimental evidence for 10 of these contrast modes. In particular, some of these modes allow for identification of the two surface reconstructions while others do not. This variety in appearances provides an explanation for the seemingly contradicting observations in the literature. Based on a detailed investigation of the influence of tip termination and interaction regime, we further analyse the existence of the row-pairing reconstruction.

(Some figures may appear in colour only in the online journal)

1. Introduction

Calcium carbonate ($CaCO_3$) is one of the most abundant simple salts in nature [1]. It is found in the shells of molluscs such as slugs or sea shells, where it constitutes the predominant component [2]. Especially calcite, the most stable polymorph of $CaCO_3$, when combined with organic material in an organic/inorganic mixture, forms materials with both outstanding material properties and amazing complexity. These biominerals, which are formed in the process of biomineralisation, have been the focus of a large number of studies during the last few decades [3].

In terms of application-oriented aspects, calcium carbonate is used in many industrial products such as paints, paper, chemicals and cement as well as cosmetics and pharmaceuticals [4]. Due to its birefringence [5] it is furthermore present in optical devices [6]. Moreover, calcium carbonate has been discussed as a possible origin for the homochirality of life [7, 8]. This aspect became evident from studies involving chiral amino acids, demonstrating enantiospecific adsorption [9] as well as enantiospecific influence on the macroscopic crystal growth [10, 11].

The most common macroscopic form of calcite is the cleavage rhombohedron, which is terminated by the most stable cleavage planes, the ($10\bar{1}4$) surfaces. This surface has been investigated in numerous studies, using experimental techniques such as low-energy electron diffraction (LEED) [12], x-ray photoelectron spectroscopy (XPS) [12], x-ray scattering [13], x-ray reflectivity [14], grazing incidence x-ray diffraction (GIXRD) [15] or atomic force microscopy (AFM) [16–22] as well as by theoretical

[1] Present address: Dr Eberl MBE-Komponenten GmbH, Gutenbergstraße 8, D-71263 Weil der Stadt, Germany.

calculations [23–29]. Several authors have reported on the existence of a (2 × 1) reconstruction, which has been discussed controversially in the literature. Nowadays, the (2 × 1) reconstruction is confirmed as a true surface property. Interestingly, AFM investigations have frequently revealed another surface reconstruction, referred to as 'row pairing'. A critical discussion of this reconstruction including a model accounting for the physical origin is still lacking in the literature.

During the last few decades, the non-contact atomic force microscope (NC-AFM) [30] evinced to be a most powerful tool for the real-space investigation of non-conducting substrates. In particular, the frequency-modulated non-contact mode [31] has presented resolution at the atomic scale on a routine basis [32]. Using NC-AFM, it has been possible to map the atomic structure of the calcite cleavage plane both in vacuum [33, 16] and liquid [17] environments. In all studies, the atomic lattice and sometimes even point defects have been resolved. However, different contrasts have been observed, which have been ascribed to be both scan-angle- [33] and distance-dependent [16]. In another study, the tip termination has been accounted for imaging different chemical species [17].

In this paper, we demonstrate that the NC-AFM contrasts reported so far only represent a minor fraction of possible contrasts on the calcite $(10\bar{1}4)$ cleavage plane. Furthermore, we will critically discuss the existence of the row-pairing reconstruction. This paper will first review the calcite bulk and $(10\bar{1}4)$ surface properties in section 2, with a special focus on AFM investigations. Section 4 describes a new contrast classification scheme, which is deduced from our own and the literature NC-AFM data. This contrast classification scheme encompasses a total of 12 different contrasts, and 10 of them have been observed experimentally so far. The contrast modes will be related to the calcite surface properties and will be discussed in terms of tip–sample distance and tip termination dependence in section 5.

2. Bulk and $(10\bar{1}4)$ surface properties

Calcite, the most stable polymorph of calcium carbonate ($CaCO_3$), crystallizes in a trigonal crystal system (rhombohedral holohedral $\bar{3}2/m$) and its symmetry is described by the space group $R\bar{3}c$ [1]. Two more modifications of $CaCO_3$ have been found in nature [2], namely aragonite and vaterite. Aragonite, which exhibits an orthorhombic crystal structure described by the space group *Pmcn*, is thermodynamically unstable and alters on the timescale of centuries to calcite. The second metastable phase, vaterite, forms a hexagonal crystal system described by the space group $P6_3/mmc$ and converts much more rapidly to calcite or aragonite. Therefore, its appearance in nature is rare. Additionally, at least five synthetic modifications, calcite I–V, are known to transform at high pressure and/or high temperature [34].

$CaCO_3$ is composed of calcium ions and carbonate (CO_3) groups. Inside each carbonate group, covalent bonds are formed between the carbon and oxygen atoms. The interaction between each carbonate group with the surrounding calcium atoms is of strong ionic character. Usually, the charge states of these two species are characterized as Ca^{2+} and CO_3^{2-} [35].

Table 1. Dimensions for the different unit cells used to describe the calcite crystal structure. Values are taken from [1, 2, 39]. The relevant description for this paper is marked in italic.

	Structural	Pseudo	Morphological
Rhombohedral axes			
a_{rh} (Å)	6.38	6.42	12.85
α_{rh} (deg)	46.08	101.92	101.92
Most stable plane	(211)	(100)	(100)
Hexagonal axes			
a_{hex} (Å)	*4.99*	9.98	19.96
c_{hex} (Å)	*17.06*	8.53	17.06
Most stable plane	*(10$\bar{1}$4)*	(10$\bar{1}$1)	(10$\bar{1}$1)

The bulk unit cell of calcite is a rhombohedron with side length $a_{rh} = 6.375$ Å and interaxial angle $\alpha_{rh} = 46.08°$ [1, 2]. This is the primitive unit cell, usually named the structural or acute unit cell. Often, the hexagonal representation of the structural unit cell with sides of length $a_{hex} = 4.9896$ Å and $c_{hex} = 17.0610$ Å is chosen in the literature. In the hexagonal nomenclature, the most stable cleavage plane is denoted as a $(10\bar{1}4)$ surface. In this work, all directions are referenced to this hexagonal nomenclature unless explicitly stated.

Two more unit cells are occasionally used in the literature, often causing confusion in naming bulk directions and surface planes. It has been speculated in 1965 [36] that this confusion has originated from the initial description of the calcite structure by Bragg in 1914 [37, 38], where a comparison to a halite structure results in a rhombohedral calcite unit cell with side length $a_{rh,pseudo} = 6.42$ Å and interaxial angle $\alpha_{rh,pseudo} = 101.55°$. This unit cell is, however, not a true bulk unit cell, as it does not account for the different orientations of the CO_3 groups. After realizing this mistake, a morphological rhombohedral unit cell has been proposed in the literature, where the side length of the pseudo unit cell is doubled to $a_{rh,morph} = 12.85$ Å. This rhombohedral unit cell nicely describes the macroscopic crystal shape terminated by the most stable crystal planes, in this system denoted as $(100)_{morph}$. Both of these unit cells can be expressed in terms of hexagonal coordinates, which makes a total of six different descriptions present in the literature as summarized in table 1.

2.1. $(10\bar{1}4)$ *surface properties*

The most stable cleavage plane of calcite is the $(10\bar{1}4)$ surface. Upon cleaving a bulk calcite crystal along this plane, the fewest Ca–O bonds are broken [23]. The surface energy is calculated to 590 mJ m^{-2} [23] and is smallest compared to other calcite crystal surfaces [40]. Furthermore, the surface has a non-polar character as the same number of ions is present on this cleavage plane.

Within the $(10\bar{1}4)$ surface both calcium atoms and carbonate groups form a rectangular unit cell with dimensions of 4.99 × 8.10 Å^2. These dimensions are calculated from the crystallographic bulk data and have been confirmed within

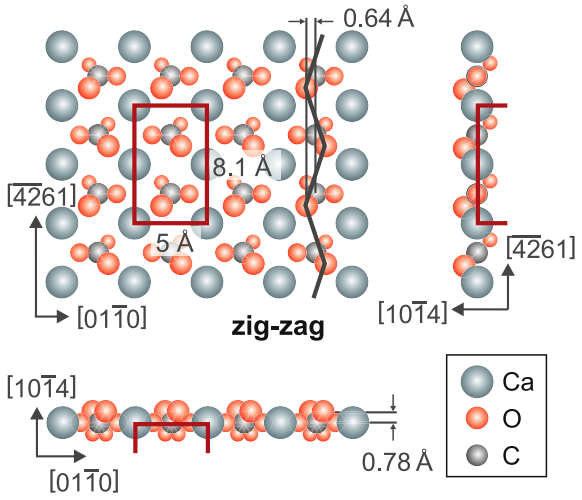

Figure 1. Bulk-truncated structure of the calcite (10$\bar{1}$4) surface including projections along the [10$\bar{1}$4], [01$\bar{1}$0] and [$\bar{4}$261] directions. The unit cell, the zigzag of the topmost oxygen atoms and various dimensions are included.

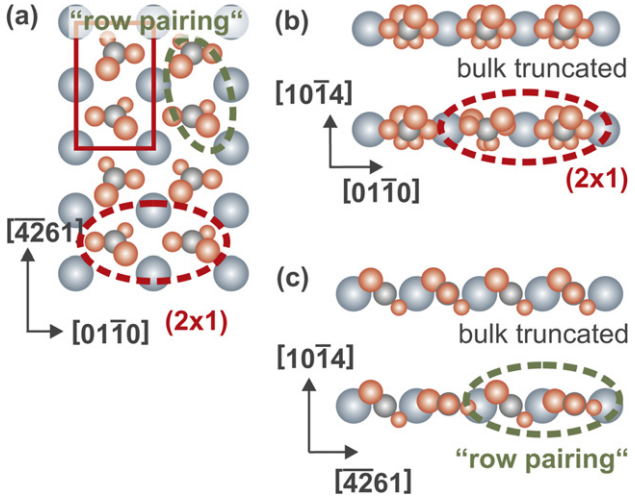

Figure 2. Reconstructions of the $CaCO_3$(10$\bar{1}$4) surface. (a) Top view showing both the (2 × 1) and the row-pairing reconstruction. (b) Side view of the (2 × 1) and (c) row-pairing reconstruction. The (2 × 1) reconstruction is drawn according to calculations by Rohl *et al* [24], while the row-pairing reconstruction is depicted following the model proposed by Jin *et al* [19].

Table 2. Surface dimensions of the bulk-truncated calcite (10$\bar{1}$4) surface. Values are calculated from the crystallographic bulk values [39].

Unit cell:		
$\vec{a} = [01\bar{1}0]$	a	4.9896 Å
$\vec{b} = [\bar{4}261]$	b	8.0955 Å
Carbonate groups:		
C–O distance	d_{C-O}	1.2815(6) Å
Angle to plane	α_{CO_3}	44.63°
O-plane distance	$d_{O-plane}$	0.7797 Å
Zigzag amplitude	A_{zigzag}	0.6408 Å

the experimental error by early LEED [12] and AFM [18] experiments. The unit cell vectors $\vec{a}$ and $\vec{b}$ of the surface unit cell are oriented along the [01$\bar{1}$0] and [$\bar{4}$261] crystallographic directions, respectively. A graphical representation of the truncated bulk structure is given in figure 1.

Two carbonate (CO_3) groups are located within the unit cell. In the truncated bulk structure, the carbon atoms of the CO_3 groups are perfectly centred between two Ca ions along the [01$\bar{1}$0] direction and the carbon atoms are equally spaced along [$\bar{4}$261]. Both carbonate groups are rotated by 44.63° with respect to the surface plane such that one of the three oxygen atoms protrudes from the plane, one lies in the plane and one is beneath the plane. The vertical distance of the protruding oxygen atoms to the surface plane amounts to 0.78 Å, as calculated from a C–O distance [39] of 1.2815(6) Å. Furthermore, the two carbonate groups inside one surface unit cell are rotated with respect to each other by 180°; thus the upmost oxygen atom points either to the left or to the right. Following the position of these protruding oxygen atoms, a zigzag line becomes apparent and is included in figure 1. The amplitude of this zigzag line is calculated as 0.64 Å.

All relevant dimensions calculated from the bulk-truncated surface structure are summarized in table 2. These values are calculated from the crystallographic bulk values and the C–O distance determined by Effenberger *et al* [39].

2.2. *Surface reconstructions*

From early AFM [18] and LEED [12] experiments, two reconstructions of the calcite (10$\bar{1}$4) surface have been reported, one identified as a (2 × 1) reconstruction and the second referred to as 'row pairing'. The existence of the (2 × 1) reconstruction has been under debate, but is nowadays accepted as a true surface property [24, 12, 41]. In contrast, a similarly detailed discussion on the existence of the row-pairing reconstruction is lacking in the literature. This might be due to the fact that this reconstruction is virtually omnipresent in AFM studies [18, 20, 19, 17, 16, 42, 21]. However, as the argument regarding this reconstruction is based solely on AFM data, it is worthwhile to initiate a critical discussion of the existence of the row-pairing reconstruction.

The current description of each of these two reconstructions is separately depicted in figure 2. The models follow work performed by Rohl *et al* [24] for the (2 × 1) reconstruction and by Jin *et al* [19] for the row pairing. In addition to these surface reconstructions, intense relaxations involving atom displacements and carbonate group rotation within the upper atomic layers have been revealed by both theoretical investigations [23, 25, 24] as well as experimental studies [15, 14, 13].

The (2 × 1) reconstruction has been discussed controversially in the literature but is nowadays accounted a true surface property [24, 12, 41]. This reconstruction doubles the unit cell length along the [01$\bar{1}$0] substrate direction, leading to a (2 × 1) supercell (see the model in figure 2(b)). Evidence for a (2 × 1) reconstruction has first been given by Stipp *et al* [12] in 1991, using LEED data from samples cleaved in air. Subsequent experimental studies using contact AFM in

liquid by Rachlin *et al* [18] and Liang *et al* [21] as well as non-contact AFM in a liquid environment by Rode *et al* [17] did, however, not reveal the (2 × 1) reconstruction. Likewise, in a GIXRD study performed by Magdans *et al* in N_2 and a humid atmosphere [15], the (2 × 1) reconstruction has not been observed either. In the latter study, however, it remains unclear to us whether a (2 × 1) reconstruction would have been identifiable at all. Regarding NC-AFM imaging, Schütte *et al* [16] have first pointed out that the visibility of the (2 × 1) reconstruction is influenced by the imaging conditions. This work has demonstrated that the visibility of the (2 × 1) reconstruction depends on the sensed interaction regime, thereby providing experimental evidence for the existence of this reconstruction.

Rohl *et al* [24] have presented *ab initio* calculations, which included evidence for a (2 × 1) reconstruction. The existence has been deduced from 'the presence of an imaginary phonon mode at $(\frac{1}{2}, 0)$ in the 2D Brillouin zone for a single surface cell' [24] and in the same study, the exothermic energy change upon forming has been calculated as 3 meV. Furthermore, they pointed out that previous calculations might not have been able to resolve the reconstruction. In a very recent study by Akiyama *et al* [41], however, the formation of a (2 × 1) reconstruction has been reported to yield a surface energy slightly larger by 0.01 J m^{-2}. Among other theoretical studies, the calcite surface has been investigated before by de Leeuw *et al* [43] and Wright *et al* [25] using atomistic simulations. In another theoretical study by Kristensen *et al* [23] in 2004, the surface including steps and kink sites has been modelled by means of parameterized interatomic potentials. The relaxation of carbonate groups at the most prominent [$\bar{4}$401] and [$\overline{48}$ 12 1] step edges has been reported to have an intense influence on the orientation of carbonate groups on the terraces next to the step edges. Specifically, the relaxation has been observed to lead to a (2 × 1) reconstruction on the adjacent terraces, but the effect is expected to be negligible for terrace sizes larger than 4.5 nm.

First evidence for the row-pairing reconstruction has been given by Rachlin *et al* [18] from contact AFM data in 1992. In these data, the row-pairing reconstruction has become apparent from a height difference of the two features imaged inside the surface unit cell. Sometimes, the height difference leads to the impression of paired rows, which is the origin of the notation 'row paring'. The finding of Rachlin *et al* has been reproduced in consecutive experiments by Stipp *et al* [20] and Jin *et al* [19] using contact AFM in liquid and atmospheric environment, by Rode *et al* [17] using NC-AFM in a liquid environment and by Schütte *et al* [16] using NC-AFM under ultra-high vacuum (UHV) conditions. In contrast, the row-pairing reconstruction has neither been observed in experiments by Fenter *et al* [14] using x-ray reflectivity and by Geissbühler *et al* [13] using x-ray scattering in a liquid environment, nor by Magdans *et al* [15] using GIXRD in N_2 and humid atmosphere. This fact readily stimulates the question whether the experimental set-up has not been sensitive enough to detect the row-pairing reconstruction, or whether the row pairing is a tip-induced scanning artefact in AFM experiments.

A possible model explaining the row-pairing reconstruction has been given by Jin *et al* [19]. In this model it is assumed that the carbonate groups rotate along the [01$\bar{1}$0] substrate direction. Using the imaged height difference in contact AFM data and simple trigonometry, an angle of (35 ± 5)° has been calculated, by which every second carbonate group is assumed to be rotated. A visualization of the rotation according to this model is given in figure 2(c). However, we stress the ambiguity in measuring heights with the AFM at the atomic scale.

In summary, the existence of the (2 × 1) reconstruction has been confirmed experimentally by both LEED [12] and various AFM measurements. This reconstruction is, therefore, accepted as a true surface property. The row-pairing reconstruction, in contrast, seems still to be disputable, especially because evidence has so far only been presented in AFM studies. Section 3 will present extensive NC-AFM results acquired under UHV conditions. In this environment, we investigate the pristine surface as we can exclude any surface contamination, especially an adsorbed water film. Both reconstructions manifest themselves in numerous different contrast modes, while they are absent in others as will be discussed in sections 4 and 5. This variability in appearance makes unambiguous data interpretation difficult and provides an explanation for the controversy in the literature.

3. Methods

All experiments were carried out under UHV conditions at a base pressure better than 1 × 10^{-10} mbar. Calcite single crystals of optical quality were bought from Korth Kristalle GmbH (Altenholz (Kiel), Germany) and were mechanically cut to the desired crystal size. After introduction into the UHV system, they were cleaved by scoring lines with a scalpel [44] and annealed for about 1.5 h to a maximum temperature of about 450 K in order to remove surface charges. The main surface orientation is carefully determined for each sample by measuring the unit cell dimensions in drift-corrected images [45]. When only identifying the unit cell dimensions, however, the carbonate group orientation still remains unclear. This fact is equivalent to an unknown direction of one main surface direction. We indicate this fact by adding two arrows to the main substrate orientation in all NC-AFM images.

In NC-AFM, the force between the sample surface and a tip mounted at the end of a cantilever is measured. In the herein used frequency-modulation mode [31], the cantilever is oscillated at its resonance frequency, while the tip–sample interaction leads to a shift of this frequency upon approaching the sample surface. The resulting frequency shift Δf is the main measurement signal and is related to the interaction force [46, 47]. The NC-AFM used in this study is a VT AFM 25 from Omicron (Taunusstein, Germany) operated in the frequency-modulated non-contact mode. The frequency shift Δf is measured using an easyPLL plus phase-locked loop from Nanosurf (Liestal, Switzerland). The NC-AFM system is equipped with a home-built atom-tracking system [48] for utmost drift stability.

All presented data are frequency shift data mapped to a green colour scale such that bright colours denote more negative Δf values than dark colours. Most NC-AFM images are acquired in the so-called quasi constant-height mode, where the bandwidth of the z feedback loop is highly reduced, such that it compensates only for thermal drift and sample tilt. In order to quantitatively rule out feedback effects, the residual z movement is calculated as the full width at half-maximum (FWHM) of the z height distribution; the corresponding values are given in this study. Other data are acquired in the true constant-height mode, where thermal drift is compensated by an atom-tracking system [48] and the z feedback is switched off. Artefacts due to the z feedback loop are completely absent in this mode. All data are unfiltered raw data unless stated otherwise. Frequency shift versus distance ($\Delta f(z)$) curves were acquired using the atom-tracking system [48]. In all $\Delta f(z)$ curves, the smallest z value is arbitrarily set to zero.

In the following discussion, we will refer to the Δf difference of on-top and hollow sites as corrugation. In contrast, the Δf difference comparing two on-top sites is called modulation. The former, thus, quantitatively describes the atomic contrast, while the latter denotes the contrast of the discussed reconstruction.

Standard Si cantilevers (type PPP-NCH from Nanosensors, Neuchâtel, Switzerland) with resonance frequencies around 300 kHz were excited to amplitudes around 10 nm. All tips were initially bombarded with Ar^+ ions to remove contaminants and the oxide layer.

4. NC-AFM contrast classification scheme

When using the AFM technique for atomic-resolution imaging, usually two sites of maximum interaction are observed inside the calcite (1×1) unit cell [21, 16, 19, 20, 18, 17, 22]. When considering the (2×1) reconstruction, the primitive surface unit cell doubles in size and, therefore, a total of four sites of maximum interaction are usually observed.

Often, the positions of maximum interaction have been assigned to the topmost oxygen atom of the carbonate groups. This assumption is based on two facts. First, the topmost oxygen atoms protrude from the surface [22] and, second, the observed surface characteristics such as a zigzag pattern or the reconstructions are assigned to the topmost oxygen atoms [22]. If these characteristics are absent, the possibility of imaging the Ca sublattice due to a different tip termination has been proposed from NC-AFM experiments in the repulsive interaction regime [17, 49].

Understanding the contrast formation in NC-AFM experiments is a delicate task, as the force interaction between tip and surface is highly dependent on the tip configuration [26, 32]. To name one example, on $TiO_2(110)$ the tip termination decides upon which surface species is imaged 'bright' and, in particular, this species is not necessarily the protruding one [50]. The interaction of Si and MgO tips with the calcite $(10\bar{1}4)$ surface has been investigated by means of *ab initio* calculations by Foster *et al* [27–29]. For an Si tip, the strongest attractive interaction has been found to originate from the topmost oxygen atoms, but for ionic tips the interaction is found to severely depend on the tip polarity. Interestingly, a zigzag pattern has been revealed even when imaging the Ca sublattice with a negatively terminated tip [29]. However, the contrast formation due to the surface reconstructions has, to the best of our knowledge, not been discussed so far. For an Si tip, the tip–sample interaction has been found to be exclusively of electrostatic nature at large tip–sample distances, where the surface ions cause a polarization of the AFM tip. At small tip–sample distances, charge transfer processes from the negatively charged surface CO_3 carbonate groups to an Si tip are found as the predominant interaction [27]. Moreover, at small tip–sample distances, an intense relaxation of the surface ions has been calculated where both the carbonate groups and calcium atoms move relative to their bulk position by up to $\sim$1 Å and the carbonate groups undergo an additional rotation [29]. This tip-induced surface relaxation might have an intense influence on the resulting AFM data.

We now introduce a contrast classification scheme, which covers all NC-AFM contrasts observed experimentally so far. All calcite $(10\bar{1}4)$ surface effects are considered and usually represent themselves in more than one contrast mode. For the contrast classification scheme, the (2×1) surface unit cell is considered as the primitive unit cell. Inside this (2×1) supercell, up to four sites of maximum attractive interaction are observed. When using the NC-AFM, these sites are apparent as up to four 'bright spots' in the Δf data, as they will be called in the following.

The scheme is divided into three classes. One class represents the most basic appearance, referred to as base contrast **B**. The second class discusses the vertical contrasts (namely $\mathbf{V}_1$ to $\mathbf{V}_5$). The vertical contrast modes cover differences in interaction strength, namely in differences of the frequency shift Δf. The third class encompasses the lateral contrasts (namely $\mathbf{L}_1$ to $\mathbf{L}_6$). The lateral contrast modes discuss lateral effects such as shifts of, or connections between, the bright spots. Therefore, all contrasts are classified by the appearance of the four bright spots in the Δf channel. This discussion can be made, regardless of the chemical nature of the bright spots. A graphical representation of all contrast modes is given in figure 3. A combination of a vertical with a lateral contrast mode is often observed and examples will be presented in section 4.4.

*4.1. Base contrast **B***

The base contrast **B** is formed by four spots of equal brightness, size and separation. Consequently, neither the (2×1), nor the row pairing reconstruction nor the zigzag pattern are visible in this contrast mode. A similar contrast has been observed in the repulsive regime under liquid conditions [17], where the lack of the zigzag pattern has been accounted for imaging the Ca sublattice. However, *ab initio* calculation using a negatively charged tip also reproduced the zigzag when imaging the Ca sublattice [29].

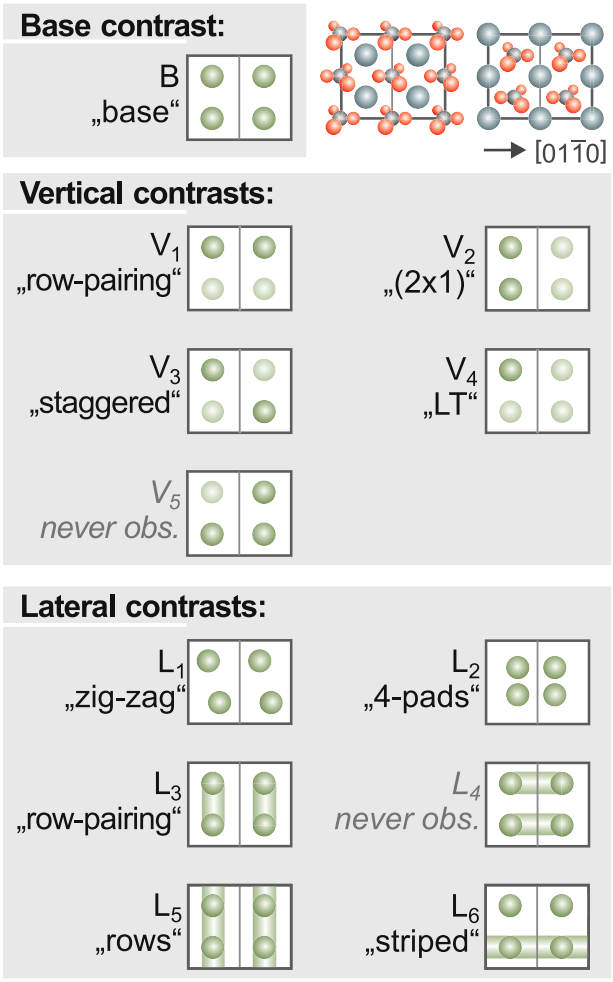

Figure 3. Classification scheme describing the NC-AFM contrasts on $CaCO_3(10\bar{1}4)$ surfaces observed so far. Up to four interaction maxima are present within the (2 × 1) surface unit cell. The appearance of these maximum positions divide the classes into the 'base' contrast mode **B**, vertical contrast modes $\mathbf{V}_i$ and lateral contrast modes $\mathbf{L}_i$.

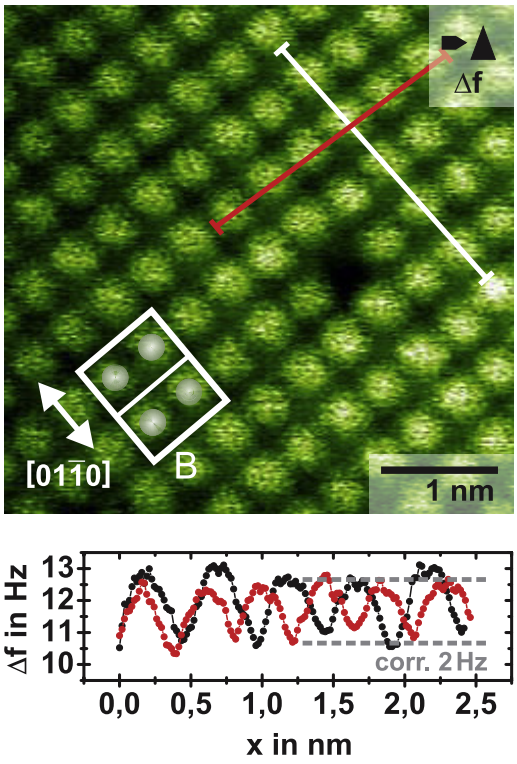

Figure 4. Contrast mode **B**: four sites of maximum interaction are revealed inside the (2 × 1) unit cell. The maxima are identical in interaction strength, size and separation. A most sharp AFM tip is demonstrated in these data by resolving a point defect. The quasi constant-height mode is used and the residual z movement is as small as 6.6 pm, as revealed from the FWHM of the height distribution (not shown).

Exemplary data are presented in figure 4, where a frequency shift Δf image is depicted. The superimposed (2 × 1) unit cell illustrates the four spots of equal interaction strength and equidistant spacing. Each spot exhibits a disc-like outline. The corrugation, which is defined as the Δf difference between the on-top and hollow sites, in this image is of the order of 2 Hz as directly visible from the line profiles. The image is acquired in the quasi-constant-height mode with a residual z movement of about 7 pm as determined by the full width at half-maximum (FWHM) of the height distribution (not shown). Thus, feedback loop artefacts are expected to be negligible. Furthermore, the single defect resolved in figure 4 demonstrates the sharpness of the AFM tip. As will be outlined later, our analysis suggest that this contrast might be found in specific interaction regimes only.

4.2. Vertical modes $\mathbf{V}_1$ to $\mathbf{V}_5$

The class of vertical contrast modes encompasses all contrast modes that differ in the vertical interaction strength at the four spot sites. In the Δf measurement channel, this difference is often referred to as 'brightness', in the topography channel it is apparent as imaged height. No lateral effects are considered in this class. For the vertical contrast, we only consider a simple binary scheme: strong or weak interaction at the four spots inside the (2 × 1) surface unit cell. In the Δf data, this is found as bright and dark spot sites. Within this scheme, combinatorial analysis reveals a total of six possible combinations[2]. One of these possibilities is the already discussed base contrast **B**, where the interaction strength at all spot sites is similar. The other cases are the vertical modes $\mathbf{V}_1$ to $\mathbf{V}_5$, where either one, two or three spots appear bright, with the other three, two or one dark, respectively.

The first mode $\mathbf{V}_1$ is the well-known row-pairing contrast, where every second row is imaged darker due to a smaller tip–sample interaction strength. With the feedback loop enabled, this contrast difference is reflected in the topography channel if the constant-Δf mode is chosen. Contrast $\mathbf{V}_1$ has been reported in the literature before, using the AFM in the contact [20] and non-contact [16, 17] mode. Figure 5 shows a typical example of the $\mathbf{V}_1$ contrast taken with an NC-AFM

[2] The symmetry properties of the substrate are neglected here. All cases bearing a mirror symmetry to each other are merged. Additionally, a translation by half a unit cell is allowed as such a translation could not be detected by the NC-AFM. Moreover, the case of all dark spots is neglected, as it cannot be distinguished from base contrast **B**.

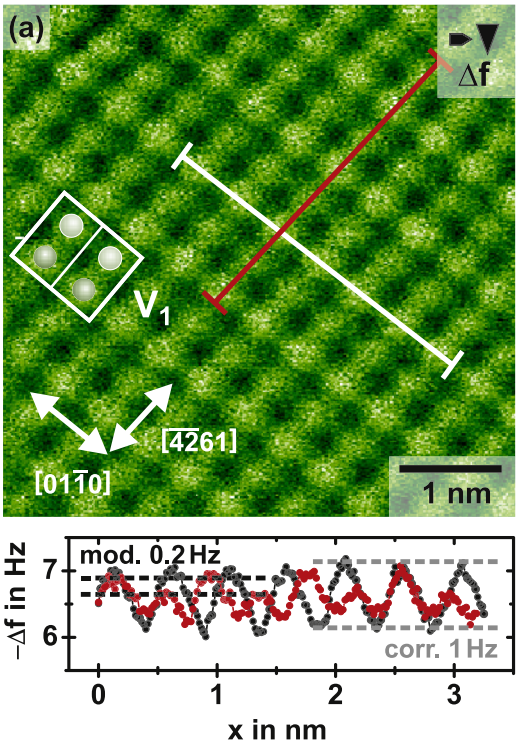

Figure 5. Experimental evidence for vertical contrast mode $\mathbf{V}_1$, the 'row-pairing' contrast. The averaged line profiles are depicted at the bottom. The residual z movement in the quasi constant-height mode was 21 pm.

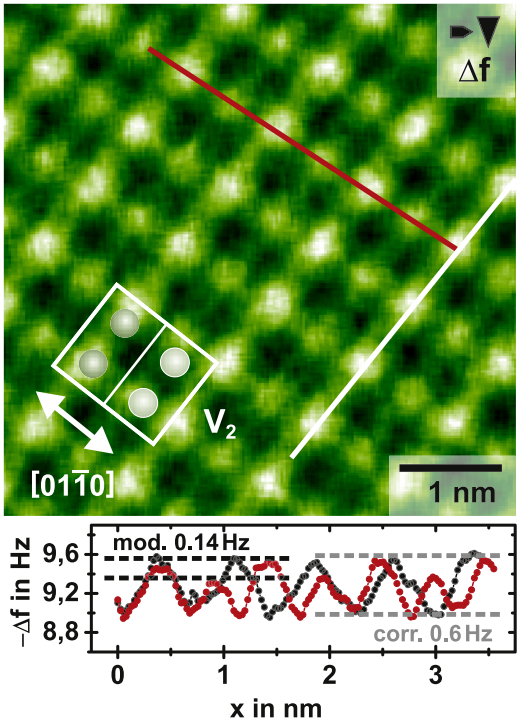

Figure 6. Experimental evidence for the vertical contrast mode $\mathbf{V}_2$, the (2×1) contrast. The image was acquired in the quasi constant-height mode, while the residual z movement is of the order of 23 pm. For visualization purposes, a five pixel mean was applied to the data.

under UHV conditions. The frequency shift image clearly presents atomic rows, alternating in interaction strength along the [$\bar{4}$261] substrate direction. In these data, the atomic corrugation, defined as the difference between the minimum and maximum value of the Δf data, has a value of about 1 Hz. In contrast, the modulation (i.e. the difference between two neighbouring maxima sites) along the [$\bar{4}$261] direction is only of the order of 0.2 Hz, as visible from the line profiles in figure 5. For the present system and parameters, this value is close to the instrumental noise level. Thus, as will be outlined in section 5, the contrast $\mathbf{V}_1$ is sometimes hardly visible, although an interaction difference is apparent at nearly all distances.

The second vertical contrast mode $\mathbf{V}_2$ is an expression of the (2×1) reconstruction. In this contrast mode, every second row along the [01$\bar{1}$0] direction alternates in interaction strength, thus doubling the unit cell length along the [01$\bar{1}$0] direction and resulting in a (2×1) superstructure. An experimental example is depicted in figure 6. In these data, the atomic corrugation is about 0.6 Hz and the modulation along the [01$\bar{1}$0] direction is only 0.14 Hz as is directly visible from the line profiles. Also in this mode, the corrugation and modulation intensity are both highly dependent on the interaction regime. The distance-dependent contrast formation of the (2×1) reconstruction has first been investigated by Schütte *et al* [16]. In the latter work small changes in the interaction regime have been observed to separate the regimes where the $\mathbf{V}_2$ contrast is visible or not. This finding will be further investigated in section 5.

In the third contrast mode $\mathbf{V}_3$, two bright spots are staggered inside the (2×1) supercell. Presumably, both reconstructions, namely the (2×1) and the row-pairing reconstruction, superimpose in this mode. The contrast is observed rarely: however, experimental evidence is given in figure 7. In these data, the atomic corrugation is of the order of 1.3 Hz, while the modulations along both substrate directions is ∼0.5 Hz. This contrast mode has not been presented before. We speculate that it is caused by a peculiar tip termination.

The fourth contrast mode $\mathbf{V}_4$, where only one of the four interaction sites inside the (2×1) unit cell is imaged bright, has been observed so far at reduced temperatures only by Schütte *et al* [16]. One exemplary image acquired at a sample temperature of about 110 K is presented in figure 8. The contrast reproduces both the (2×1) reconstruction along [01$\bar{1}$0] as well as the row-pairing reconstruction along the [$\bar{4}$261] direction. This contrast mode might be considered as a superposition of both modes, as was suggested before for contrast mode $\mathbf{V}_3$. Rohl *et al* [24] reported that the formation of the (2×1) reconstruction is exothermic with $\Delta E = 3$ meV. Consequently, a thermal averaging of the (1×1) and (2×1) configurations is expected at room temperature due to the tiny energy difference. However, upon decreasing the temperature, the occupation probabilities for both configurations might be influenced, leading to a more pronounced appearance of the (2×1) reconstruction in NC-AFM images acquired at low temperatures.

The fifth contrast mode $\mathbf{V}_5$ has not been observed experimentally so far. It can be considered as an inversion

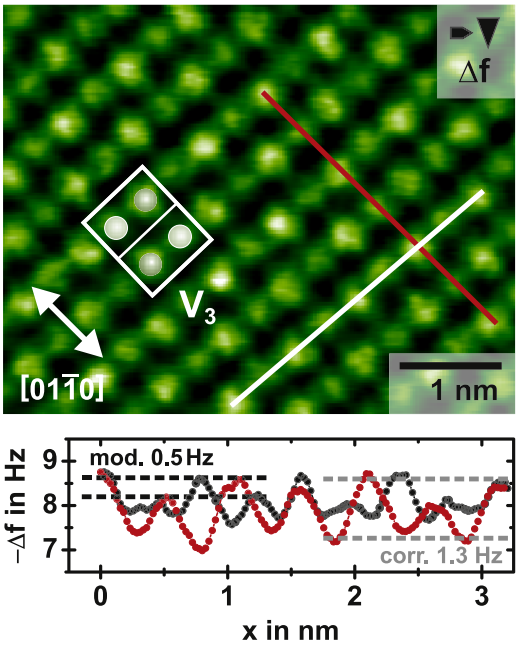

Figure 7. NC-AFM data presenting the vertical contrast mode $\mathbf{V}_3$. The quasi constant-height imaging mode was chosen with a residual z movement of about 12 pm. For visualization purposes, a five pixel mean was applied to the data.

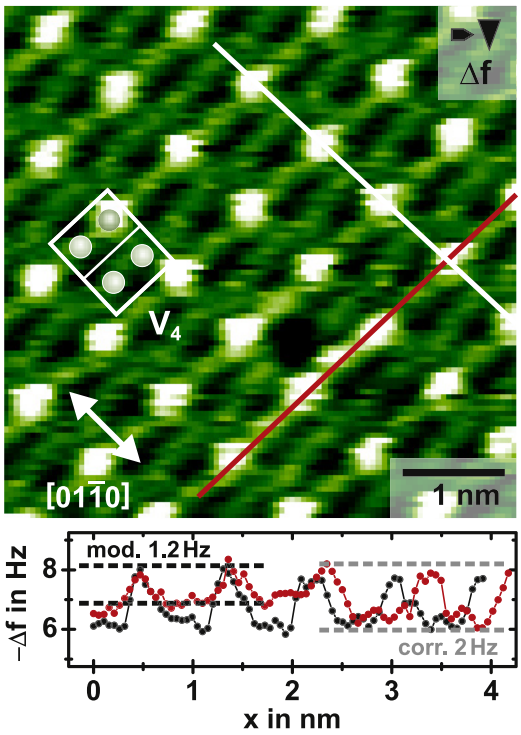

Figure 8. NC-AFM image depicting the vertical contrast mode $\mathbf{V}_4$. The image was acquired at a sample temperature of 110 K. The residual z movement is determined as 54 pm. The image is adapted from [16].

of contrast $\mathbf{V}_4$, where three spots are imaged bright and only one is dark. This mode is included in this discussion for consistency reasons.

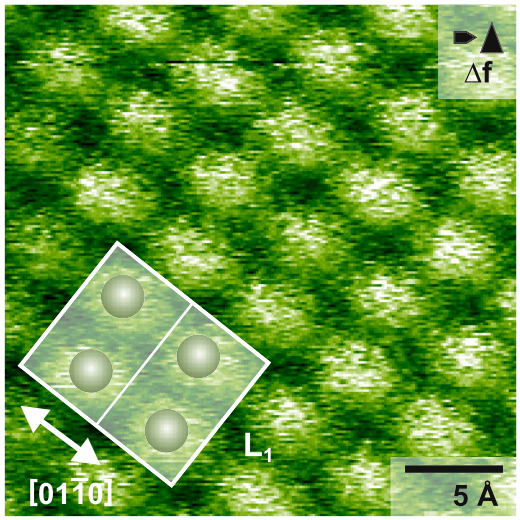

Figure 9. Experimental evidence for lateral contrast mode $\mathbf{L}_1$. The image was acquired in the quasi constant-height mode with a residual z movement of about 19 pm.

4.3. Lateral contrasts $\boldsymbol{L}_1$ to $\boldsymbol{L}_5$

Besides the differences in interaction strength, lateral effects such as shifts of, or connections between, spots are frequently observed in AFM imaging of the calcite $(10\bar{1}4)$ surface. These effects form the third class of contrast modes, which are herein named lateral modes $\mathbf{L}_1$ to $\mathbf{L}_6$. In contrast to the vertical modes, the lateral modes do not follow any combinatorics and, thus, they cover all contrasts observed up to now. Consequently, this list might still be incomplete.

One of the well-known lateral contrast modes is the contrast mode $\mathbf{L}_1$, where every second spot aligned along the $[\bar{4}2\bar{6}1]$ direction is laterally shifted. This shift leads to the characteristic zigzag pattern, which has been observed before using the AFM in contact [21] and non-contact [16, 17] modes. One typical example obtained with the NC-AFM is shown in figure 9. The zigzag pattern has been related to the orientation of the topmost oxygen atoms of the CO_3 groups. When considering the bulk-truncated model, this zigzag exhibits an amplitude of 0.64 Å. Interestingly, experimental values ranging from 0.35 to 1.05 Å have been reported [21]. From the data in figure 9, we find a zigzag amplitude of about 0.6 Å. For an AFM tip at positive potential, the interpretation of imaging the protruding oxygen atoms has been corroborated by Foster *et al* [29], where *ab initio* simulated NC-AFM images have reproduced the zigzag pattern. However, in the same work the authors also reported on a zigzag pattern when imaging the Ca sublattice with a tip at negative potential, but the zigzag amplitude is smaller. The analysis in section 5 will suggest that this contrast mode is dependent on both tip termination and tip–sample distance.

In the second lateral contrast mode $\mathbf{L}_2$, herein named the 'four-pad' mode, all four spots appear to move to the unit cell centre. This shift leads to the appearance of a pad-like structure and is, again, related to both the (2×1) and the row-pairing reconstruction. This mode has been

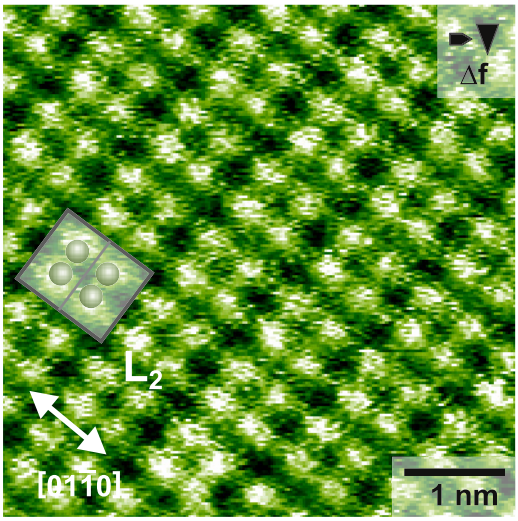

Figure 10. Representative image revealing the lateral contrast mode $\mathbf{L}_2$. The image was acquired in the quasi constant-height mode, while the residual z movement was of the order of 13 pm. The data are adapted from [16].

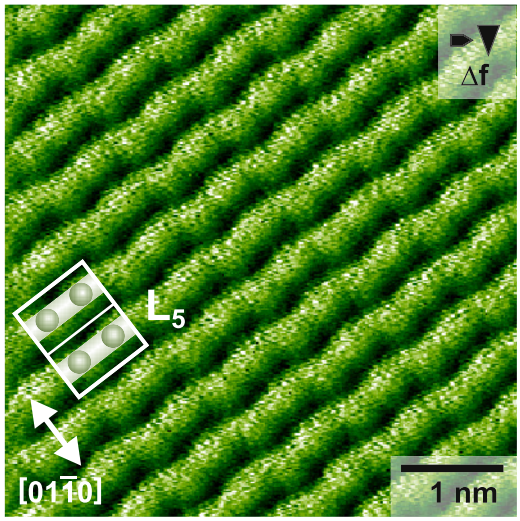

Figure 12. Experimental example for the lateral contrast mode $\mathbf{L}_5$. The z movement amounts to about 47 pm, which is the largest in all data presented herein.

observed before by Schütte *et al* [16] using the NC-AFM. A representative NC-AFM image is given in figure 10.

The third and fourth lateral contrast modes are each characterized by a pairing of two spots, either along the [$\bar{4}$261] direction in contrast mode $\mathbf{L}_3$ or along the [01$\bar{1}$0] direction in contrast mode $\mathbf{L}_4$. The lateral contrast mode $\mathbf{L}_3$, where the pairing occurs along the [$\bar{4}$261] direction, is clearly related to the row-pairing reconstruction. In this mode, the appearance of a pairing is directly visible. Figures 11(a) and (b) depict representative NC-AFM data for this contrast mode. The data in (b) represent an extreme manifestation of this contrast mode, where the pairing intensity leads to merging of the two original spots. This mode will be related to a particular tip termination in section 5. In contrast, contrast mode $\mathbf{L}_4$ has not been observed experimentally so far. It represents a pairing along the [01$\bar{1}$0] direction and is, consequently, linked to the (2 × 1) reconstruction. This contrast mode is included for consistency only.

The two remaining lateral contrast modes $\mathbf{L}_5$ and $\mathbf{L}_6$ are characterized by continuous lines, either along the [$\bar{4}$261] direction in mode $\mathbf{L}_5$ or along the [01$\bar{1}$0] direction in mode $\mathbf{L}_6$. In mode $\mathbf{L}_5$, which suggests a relation to the row-pairing reconstruction, continuous lines running along the [$\bar{4}$261] surface direction are observed. Frequently, no vertical modulation is observed along each line, but a slight lateral zigzag. A typical NC-AFM image is reproduced in figure 12. The contrast has been presented before using the NC-AFM technique [16], but only in a specific interaction regime. Therefore, this contrast mode appears to be highly dependent on the interaction regime sensed. Additionally, the residual z movement in figure 12 is the largest of all herein presented data. Thus, a feedback loop artefact in an intermediate constant-height/constant-Δf mode might also intensify this contrast.

In lateral contrast mode $\mathbf{L}_6$, one straight line alternates with individually resolved spots. The straight lines are oriented along the [01$\bar{1}$0] direction, while the alternation runs

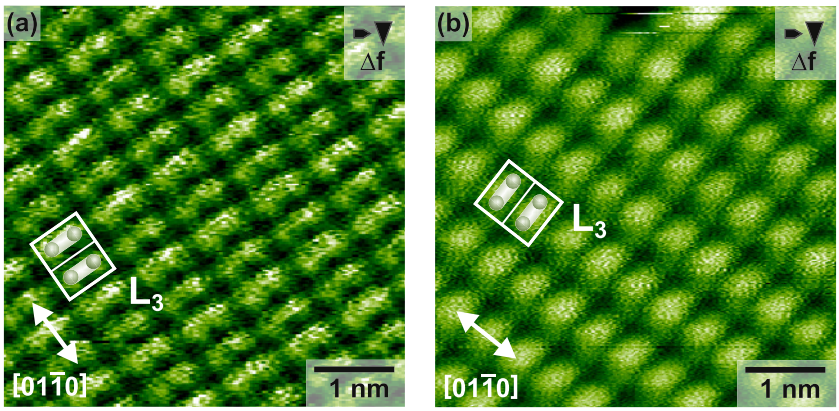

Figure 11. Experimental examples for lateral contrast mode $\mathbf{L}_3$. Both images were acquired in the quasi constant-height mode with residual z movements of (a) 21 pm and (b) 21 pm.

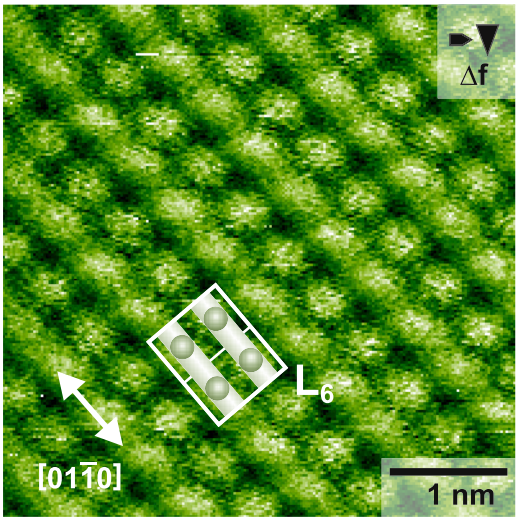

Figure 13. NC-AFM data representing lateral contrast mode $\mathbf{L}_6$. The residual z movement in the quasi constant-height mode amounts to about 12 pm.

along [$\bar{4}$261]. Consequently, this contrast mode is also linked to the row-pairing reconstruction. A representative NC-AFM image is presented in figure 13.

4.4. Combination of contrast modes

Besides the clear separation between lateral and vertical contrast modes, we frequently observe a combination of a lateral with a vertical mode. Figure 14 depicts three examples, where a vertical contrast mode combines with a lateral mode in each NC-AFM image.

The concept of our contrast classification scheme allows for an unambiguous identification of the contrast mode separated into a vertical and a lateral mode. However, we want to stress that for this identification the main surface directions need to be known. These are usually deduced from measuring the unit cell sizes in drift-corrected [48, 45] AFM images.

Figure 14(a) clearly reveals a combination of modes $\mathbf{V}_2$ with $\mathbf{L}_3$. Thus, both the (2 × 1) and the row-pairing reconstruction are directly visible, the former as vertical mode $\mathbf{V}_2$, the latter as lateral contrast mode $\mathbf{L}_3$. The analysis in section 5 will suggest a tip-dependent formation of contrast mode $\mathbf{L}_3$. In figure 14(b), contrast mode $\mathbf{V}_1$ combines with contrast mode $\mathbf{L}_5$. The overall appearance is of a stripe-like form with the stripes running along the [$\bar{4}\bar{2}$61] substrate direction. Each contrast mode is related to the row-pairing reconstruction: however, the (2 × 1) reconstructions is not visible in this combination. This is also the case for the last contrast combination depicted in figure 14(c). Here, contrast mode $\mathbf{V}_1$ combines with mode $\mathbf{L}_6$ leading to a stripe-like appearance along the [01$\bar{1}$0] direction. The vertical contrast mode clearly demonstrates the row pairing, but the (2 × 1) reconstruction remains invisible. This contrast mode is predominantly found at small tip–sample distances.

5. Discussion

5.1. Change of contrast modes

The former classification presented a total of 12 NC-AFM contrast modes for imaging the calcite (10$\bar{1}$4) surface. Experimental evidence was given for 10 of these modes. For each contrast mode, the relation to the calcite surface properties was discussed. We conclude that both surface reconstructions manifest themselves in numerous different contrasts, which gives further firsthand evidence for the controversially discussed existence of both surface reconstructions. However, AFM data are generally dependent on the tip configuration, which may result in imaging artefacts as will be discussed further on. Furthermore, for one of the contrast modes we will find a strong influence of the tip termination on the contrast, while several other contrast modes are visible only in specific interaction regimes. Both influences, tip termination and interaction regime, will be discussed separately in the following based on experimental data. Discussing the precise influence of the tip termination on the NC-AFM contrast formation generally requires a thorough analysis based on *ab initio* modelling [26], which is, however, beyond the scope of this paper. Nevertheless, we want to note that we succeeded in resolving atomic-size defects for a large number of the mentioned contrast modes. This fact makes the influence of tip artefacts, such as multiple tips, very unlikely.

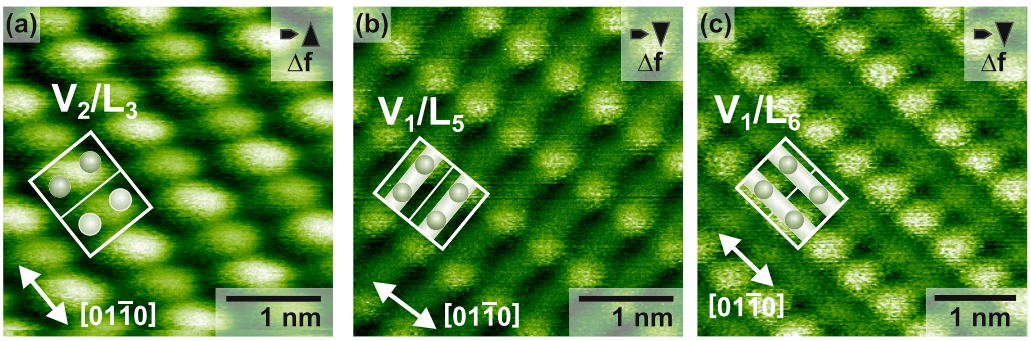

Figure 14. Examples for different combinations of vertical with lateral contrast modes. (a) and (b) are true constant-height images; the residual z movement in image (c) is about 17 pm.

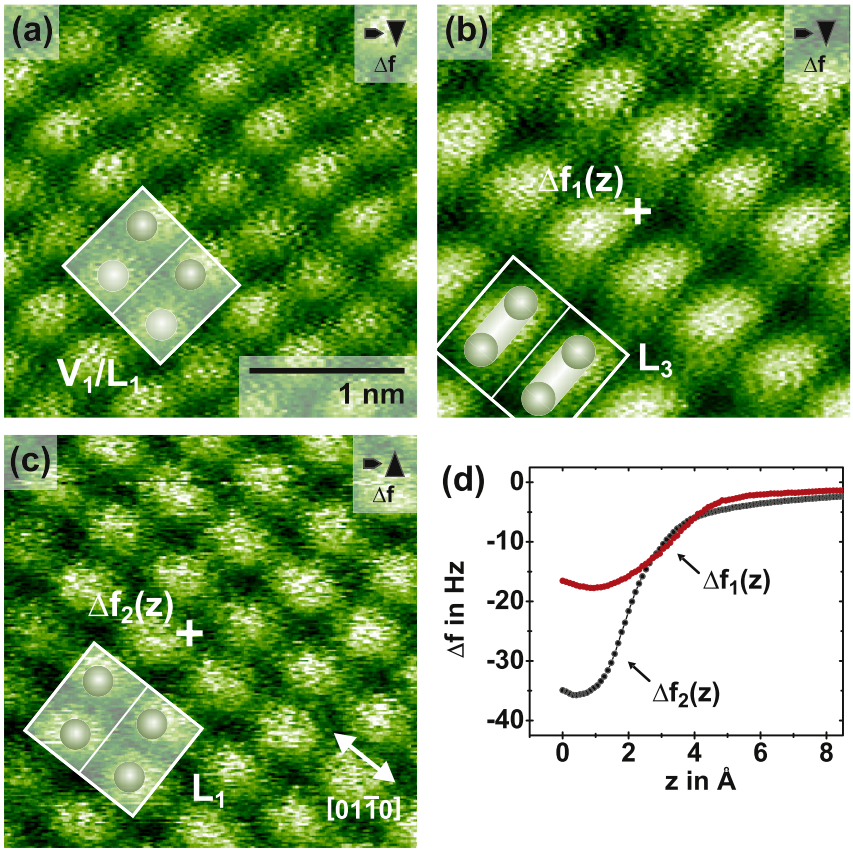

Figure 15. Tip-termination-dependent contrast formation. Tip reconfigurations were provoked by gentle tip–surface contact between images (a) and (b) as well as between (b) and (c). Averaged $\Delta f(z)$ curves are presented in (d), which were acquired at the positions indicated in images (b) and (c).

Our experimental data suggest a peculiar tip termination for the formation of the lateral contrast mode $\mathbf{L}_3$ in its extreme manifestation. This is demonstrated by the data in figure 15, where successive images acquired in a quasi constant-height mode are presented. We stress that all images are taken at roughly the same frequency shift setpoint, which was -19.5 Hz (-17 Hz, -18.5 Hz) in figures 15(a)–(c), respectively. In figure 15(a), the contrast is a combined $\mathbf{V}_1/\mathbf{L}_1$ mode. Thus, the row pairing and the zigzag are identified. Before acquiring the image in figure 15(b), a tip reconfiguration was induced by gentle contact of the tip with the surface. This reconfiguration clearly led to a change in the contrast, which is now identified as mode $\mathbf{L}_3$ in figure 15(b). This contrast mode is an expression of the row-pairing reconstruction. Neither the zigzag nor the (2×1) reconstruction is apparent in this contrast mode. Another tip reconfiguration was induced by gentle surface contact before acquiring the data in figure 15(c). Here, again, the zigzag is visible in contrast mode $\mathbf{L}_1$, while the overall contrast is comparable to the data presented in figure 15(a).

To elucidate the difference in contrast formation, $\Delta f(z)$ curve data were acquired at the indicated positions in figures 15(b) and (c). The acquisition was performed by using the repeated spectroscopy protocol [51, 48] of an atom-tracking system [48]. Both curve sets were calculated as an average of several single curves, 20 single curves for curve set $\Delta f_1(z)$ and 50 for $\Delta f_2(z)$. The lateral position of each single curve in one set was identical. The position was controlled by the atom-tracking technique to an accuracy of better than 50 pm [48].

The acquired curves present fundamental differences: most prominently the magnitude of the minimum value differs by a factor of about two. Furthermore, the curvature at an intermediate distance of $z \sim 4$ Å differs between the two curves. Consequently, these data suggest that an increased short-range chemical sensitivity leads to the contrast mode $\mathbf{L}_1$, while reduced short-range sensitivity results in contrast mode $\mathbf{L}_3$. One might speculate about a dominating influence of electrostatic and van der Waals interactions in the contrast formation of contrast mode $\mathbf{L}_3$. This finding might suggest that the appearance of the row-pairing reconstruction originates from a strong electronic reconfiguration at the sample surface.

The formation of vertical contrast modes $\mathbf{V}_1$ and $\mathbf{V}_2$ evinced to be highly dependent on the tip–sample distance. This finding results from comparing $\Delta f(z)$ curve data acquired at different sample sites as presented in figure 16. Four $\Delta f(z)$ curves acquired at four specific sample sites are analysed for the discussion: the lateral position of these sites inside the (2×1) surface unit cell is depicted in the inset. All positions are located at the sites of maximum interaction at intermediate tip–sample distances. For visualization purposes,

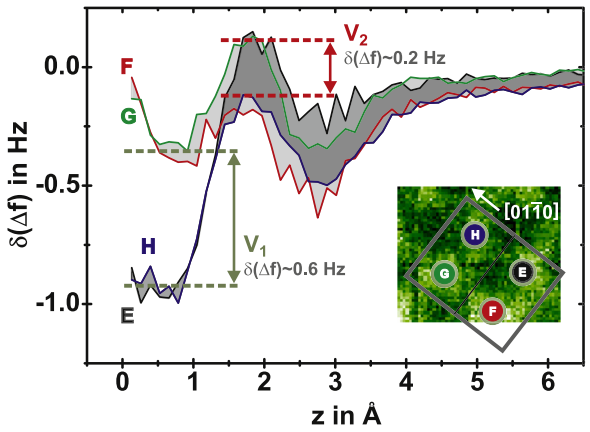

Figure 16. Tip–sample distance-dependent formation of vertical contrast modes $\mathbf{V}_1$ and $\mathbf{V}_2$. The $\Delta f(z)$ curves were acquired at the indicated tip–sample positions (capital letters E, F, G and H) by using the 3D protocol of our atom-tracking system [48]. An average curve was subtracted from these data. Thus, the tiny differences in corrugation and modulation are easily visible. The mode $\mathbf{V}_1$ (row pairing) becomes apparent by comparing curves E and F (or alternatively curves G and H). Likewise, for contrast $\mathbf{V}_2$ ((2×1) reconstruction) curves E and H (or alternatively F and G) have to be compared.

a mean interaction curve was subtracted from each curve data. This strategy does not change the relative differences when discussing the vertical contrast formation. The grey shaded areas depict the contrast mode $\mathbf{V}_2$, the (2×1) reconstruction, while the difference between these two pairs is the contrast difference in mode $\mathbf{V}_1$, the row-pairing reconstruction. At these sample sites the (2×1) reconstruction is easily identified even at large tip–sample distances. At $z \sim 2.0$ Å, the modulation of the (2×1) reconstruction is about 0.2 Hz for both curve pairs. Interestingly, the contrast decreases upon reducing the tip–sample distance. In contrast, the row-pairing reconstruction in contrast mode $\mathbf{V}_1$ is even more pronounced, while at $z \sim 0.5$ Å, the modulation is of the order of 0.6 Hz.

The formation of lateral contrasts $\mathbf{L}_1$ and $\mathbf{L}_6$ was investigated by using true constant-height data at different tip–sample distances as presented in figure 17. For both frequency shift images (a) and (b), the tip is first approached to the sample surface within the first lines (not shown), followed by a linear ramp outwards. The slow scan direction of the images is oriented from bottom to top in (a) and vice versa in (b). To identify the absolute z position, the mean value of each row is corrected for the linear ramp such that they coincide with a $\Delta f(z)$ curve acquired at one sample position. Consequently, the frequency shift images span a z range of about 4 Å as depicted in figure 17(c).

The contrast evolution in this experiment is straightforward to characterize going from large to small tip–sample distances: at large tip–sample distances ($z \sim 3$ Å), the base contrast **B** is observed. When reducing the tip–sample distance, first the zigzag contrast $\mathbf{L}_1$ evolves and, at even smaller distances, contrast $\mathbf{V}_1$ becomes apparent. Close to the minimum of the $\Delta f(z)$ curve approached in the top lines of figure 17(b), the former zigzag contrast changes into the striped appearance $\mathbf{L}_6$ combined with the vertical row-paring contrast $\mathbf{V}_1$. Thus, for the present tip termination the zigzag contrast $\mathbf{L}_1$ evolves at intermediate tip–sample distances, while the combined $\mathbf{L}_6/\mathbf{V}_1$ contrast becomes prominent close to the Δf interaction curve minimum.

5.2. (2×1) *reconstruction*

The (2×1) reconstruction is unlikely to be induced by a tip artefact due to the surface translational symmetry along the [01$\bar{1}$0] direction. This fact has been realized before by Schütte *et al* [16] and is in full agreement with LEED experiments by Stipp *et al* [12]. It should, furthermore, briefly be noted that this reconstruction does not violate the *pg* surface symmetry.

5.3. *Row-pairing reconstruction*

The (10$\bar{1}$4) surface of calcite belongs to the symmetry group *pg* (plane group no. 4), which includes glide reflections as structure isomorphisms [52, 13]. Therefore, the two carbonate groups inside the (1×1) surface unit cell are fully equivalent apart from their different orientation. In particular, the topmost oxygen atoms protrude from the surface plane spanned by Ca and C atoms by the same distance of 0.78 Å. The row-pairing reconstruction, if assumed to induce a difference between the two carbonate groups as presented in the literature [19], violates the *pg* surface symmetry. Thus, the row-pairing reconstruction breaks basic symmetry properties of the bulk-truncated surface and, firsthand, its existence should be questioned.

Although this reconstruction is virtually omnipresent in AFM studies, it has—to the best of our knowledge—not been found with any other experimental technique so far, but the number of studies is limited. As the reconstruction occurs within the surface unit cell, a tip-induced scanning artefact cannot be ruled out generally. Although the carbonate groups are identical due to the surface *pg* symmetry, their orientation to the AFM tip is different. Thus, an asymmetric tip might possibly lead to a different appearance of the two carbonate groups. However, due to the large number of observations and the varying appearances in different contrast modes, a peculiar tip termination is expected to be unlikely. As we observe the row-pairing reconstruction also at large tip–sample distances, a tip-induced surface reconfiguration appears, furthermore, to be unlikely. Nevertheless, a confirmation of the existence of this reconstruction with experimental techniques complementary to scanning probe microscopy appears highly desirable to clarify this point.

6. Conclusion

In conclusion, we discussed the NC-AFM contrast formation on the calcite (10$\bar{1}$4) surface. We presented a contrast classification scheme, encompassing a total of 12 contrast modes. Ten of these modes were found experimentally so far, while two further modes are included for consistency. One class of contrast modes, the vertical modes, cover all NC-AFM contrasts evolving from a difference in the

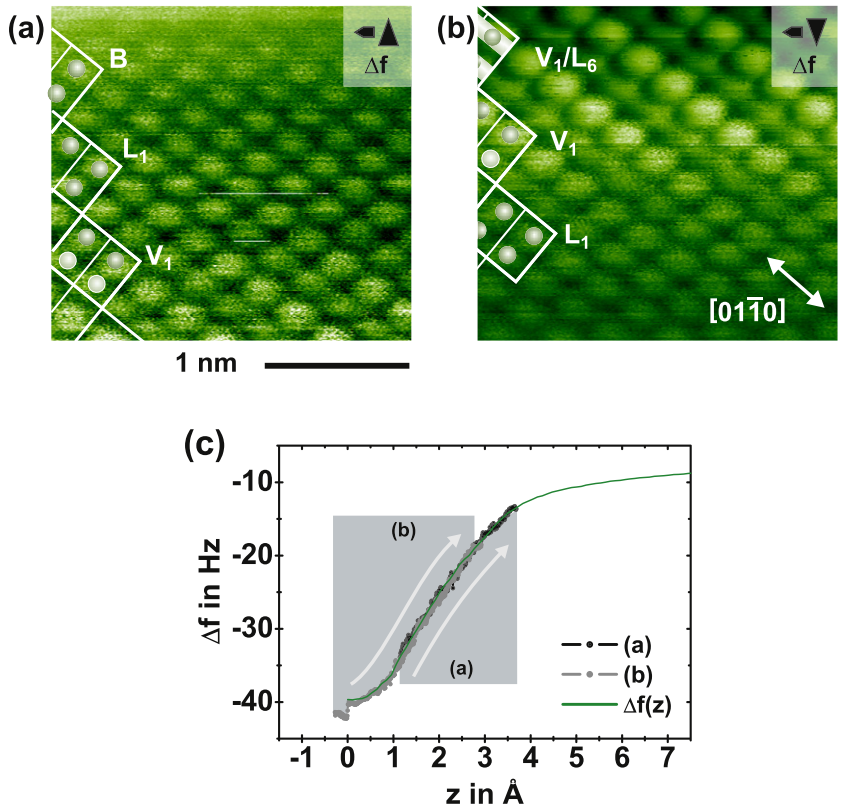

Figure 17. Tip–sample distance-dependent formation of lateral and vertical contrast modes. The frequency shift images in (a) and (b) were acquired with the distance feedback loop switched off. A linear ramp led to covering the important interaction regime of about 0–4 Å.

vertical interaction strength, while the class of lateral modes encompasses lateral imaging effects such as shifts or merging of interaction sites. Furthermore, often a combination of one vertical with one lateral contrast mode is found experimentally. The broad variety of contrasts include modes where one or both reconstructions are invisible. This observation readily provides an explanation for the seemingly controversial discussion in the literature, as distance-dependent and low-noise AFM imaging is required for resolving the reconstructions.

While the (2 × 1) reconstruction has been confirmed as a true surface property, the existence of the row-pairing reconstruction remains ambiguous, as all experimental evidence has been based on AFM so far. As a matter of principle, tip-induced artefacts, which can be ruled out for the (2 × 1) reconstruction, could manifest themselves as the row-pairing reconstruction. An independent confirmation for the existence of the row-pairing reconstruction by a complementary technique is, therefore, highly desirable. This is especially true as the existence of the row-pairing reconstruction would have far-reaching impact on the surface's symmetry properties.

Acknowledgments

We gratefully acknowledge most helpful discussions with Markus Nimmrich and Markus Kittelmann. This work has been supported by the German Research Foundation (DFG) through the DFG project KU1980/4-1.

References

[1] Reeder R J (ed) 1983 Carbonates: mineralogy and chemistry *Reviews in Mineralogy* (Washington, DC: Mineralogical Society of America)
[2] Deer W A, Howie R A and Zussman J 1992 *An Introduction to the Rock Forming Minerals* (Essex, UK: Pearson Education Limited)
[3] Addadi L and Weiner S 1992 *Angew. Chem. Int. Edn* **31** 153–69
[4] Cölfen H 2003 *Curr. Opin. Colloid Interface Sci.* **8** 23
[5] Gifford J W 1902 *Proc. R. Soc. Lond.* A **70** 329
[6] Hirano S, Yogo T and Kikuta K 1992 *Prog. Cryst. Growth Charact. Mater.* **23** 341
[7] Addadi L and Weiner S 2001 *Nature* **411** 753
[8] Hazen R M 2006 *Am. Mineral.* **91** 1715
[9] Hazen R M, Filley T R and Goodfriend G A 2001 *Proc. Natl Acad. Sci.* **98** 5487
[10] Orme C A, Noy A, Wierzbicki A, McBride M T, Grantham M, Teng H H, Dove P M and DeYoreo J J 2001 *Nature* **411** 775
[11] Wolf S E, Loges N, Mathiasch B, Panthöfer M, Mey I, Janshoff A and Tremel W 2007 *Angew. Chem. Int. Edn* **46** 5618
[12] Stipp S L and Hochella M F 1991 *Geochim. Cosmochim. Acta* **55** 1723
[13] Geissbühler P, Fenter P, DiMasi E, Srajer G, Sorensen L B and Sturchio N C 2004 *Surf. Sci.* **573** 191
[14] Fenter P, Geissbuhler P, DiMasi E, Srajer G, Sorensen L B and Sturchio N C 2000 *Geochim. Cosmochim. Acta* **64** 1221
[15] Magdans U, Gies H, Torrelles X and Rius J 2006 *Eur. J. Mineral.* **18** 831
[16] Schütte J, Rahe P, Tröger L, Rode S, Bechstein R, Reichling M and Kühnle A 2010 *Langmuir* **26** 8295
[17] Rode S, Oyabu N, Kobayashi K, Yamada H and Kühnle A 2009 *Langmuir* **25** 2850–3

[18] Rachlin A L, Henderson G S and Goh M C 1992 *Am. Mineral.* **77** 904
[19] Jin M X, Shimada E and Ikuma Y 1999 *J. Ceram. Soc. Japan* **107** 1166
[20] Stipp S L S, Eggleston C M and Nielsen B S 1994 *Geochim. Cosmochim. Acta* **58** 3023
[21] Liang Y, Lea A S, Baer D R and Engelhard M H 1996 *Surf. Sci.* **351** 172
[22] Ohnesorge F and Binnig G 1993 *Science* **260** 1451
[23] Kristensen R, Stipp S L S and Refson K 2004 *J. Chem. Phys.* **121** 8511
[24] Rohl A L, Wright K and Gale J D 2003 *Am. Mineral.* **88** 921
[25] Wright K, Cygan R T and Slater B 2001 *Phys. Chem. Chem. Phys.* **3** 839
[26] Hofer W A, Foster A S and Shluger A L 2003 *Rev. Mod. Phys.* **75** 1287
[27] Foster A S, Gal A Y, Lee Y J, Shluger A L and Nieminen R M 2003 *Appl. Surf. Sci.* **210** 146
[28] Foster A S, Gal A Y, Airaksinen J M, Pakarinen O H, Lee Y J, Gale J D, Shluger A L and Nieminen R M 2003 *Phys. Rev.* B **68** 195420
[29] Foster A S, Shluger A L and Nieminen R M 2002 *Appl. Surf. Sci.* **188** 306
[30] Binnig G, Quate C and Gerber C 1986 *Phys. Rev. Lett.* **56** 930
[31] Albrecht T R, Grütter P, Horne D and Rugar D 1991 *J. Appl. Phys.* **69** 668
[32] Barth C, Foster A S, Henry C R and Shluger A L 2011 *Adv. Mater.* **23** 477
[33] Morita S, Wiesendanger R and Meyer E (ed) 2002 *Noncontact Atomic Force Microscopy* (Berlin: Springer) pp 305–47
[34] Mirwald P W 1979 *Phys. Chem. Miner.* **4** 291
[35] Skinner A J, LaFemina J P and Jansen H J F 1994 *Am. Mineral.* **79** 205
[36] Winchell H 1956 *Am. J. Sci.* **254** 65
[37] Bragg W L 1914 *Proc. R. Soc. Lond.* A **89** 468
[38] Bragg W L 1913 *Proc. R. Soc. Lond.* A **89** 248
[39] Effenberger H, Mereiter K and Zemann J 1981 *Z. Kristallogr.* **156** 233
[40] Kerisit S, Parker S C and Harding J H 2003 *J. Phys. Chem.* B **107** 7676
[41] Akiyama T, Nakamura K and Ito T 2011 *Phys. Rev.* B **84** 085428
[42] Raina G, Gauldie R W, Sharma S K and Helsley C E 1994 *Ferroelectr. Lett. Sect.* **17** 65
[43] de Leeuw N H and Parker S C 1997 *J. Chem. Soc. Faraday Trans.* **93** 467–75
[44] Tröger L, Schütte J, Ostendorf F, Kühnle A and Reichling M 2009 *Rev. Sci. Instrum.* **80** 063703
[45] Rahe P, Bechstein R and Kühnle A 2010 *J. Vac. Sci. Technol.* B **28** C4E31
[46] Giessibl F J 1997 *Phys. Rev.* B **56** 16010
[47] Sader J E and Jarvis S P 2004 *Appl. Phys. Lett.* **84** 1801
[48] Rahe P, Schütte J, Schniederberend W, Reichling M, Abe M, Sugimoto Y and Kühnle A 2011 *Rev. Sci. Instrum.* **82** 063704
[49] Hillner P E, Manne S, Gratz A J and Hansma P K 1992 *Ultramicroscopy* **42** 1387
[50] Lauritsen J V, Foster A S, Olesen G H, Christensen M C, Kühnle A, Helveg S, Rostrup-Nielsen J R, Clausen B S, Reichling M and Besenbacher F 2006 *Nanotechnology* **17** 3436
[51] Abe M, Sugimoto Y, Custance O and Morita S 2005 *Nanotechnology* **16** 3029–34
[52] Hazen R M 2004 *Chiral Crystal Faces of Common Rock-Forming Minerals* (New York: Elsevier)